polymers

MDPI

Article

Improvement of Gas Barrier Properties for Biodegradable Poly(butylene adipate-co-terephthalate) Nanocomposites with MXene Nanosheets via Biaxial Stretching

Xionggang Wang, Xia Li, Lingna Cui, Yuejun Liu and Shuhong Fan *

Key Laboratory of Advanced Packaging Materials and Technology of Hunan Province, School of Packaging and Materials Engineering, Hunan University of Technology, Zhuzhou 412007, China; cheersun@126.com (X.W.); xiali_2019@163.com (X.L.); lncui@hut.edu.cn (L.C.); liuyuejun@hut.edu.cn (Y.L.)
* Correspondence: yangling2020@hut.edu.cn

Abstract: In order to ease the white pollution problem, biodegradable packaging materials are highly demanded. In this work, the biodegradable poly (butylene adipate-co-terephthalate)/MXene (PBAT/$Ti_3C_2T_X$) composite casting films were fabricated by melt mixing. Then, the obtained PBAT/$Ti_3C_2T_X$ composite casting films were biaxially stretched at different stretching ratios so as to reduce the water vapor permeability rate (WVPR) and oxygen transmission rate (OTR). It was expected that the combination of $Ti_3C_2T_X$ nanosheets and biaxial stretching could improve the water vapor and oxygen barrier performance of PBAT films. The scanning electron microscope (SEM) observation showed that the $Ti_3C_2T_X$ nanosheets had good compatibility with the PBAT matrix. The presence of $Ti_3C_2T_X$ acted as a nucleating agent to promote the crystallinity when the content was lower than 2 wt%. The mechanical tests showed that the incorporation of 1.0 wt% $Ti_3C_2T_X$ improved the tensile stress, elongation at break, and Young's modulus of the PBAT/$Ti_3C_2T_X$ nanocomposite simultaneously, as compared with those of pure PBAT. The mechanical dynamical tests showed that the presence of $Ti_3C_2T_X$ significantly improved the storage modulus of the PBAT nanocomposite in a glassy state. Compared with pure PBAT, PBAT-1.0 with 1.0 wt% $Ti_3C_2T_X$ exhibited the lowest OTR of 782 cc/m^2·day and 10.2 g/m^2·day. The enhancement in gas barrier properties can be attributed to the presence of $Ti_3C_2T_X$ nanosheets, which can increase the effective diffusion path length for gases. With the biaxial stretching, the OTR and WVPR of PBAT-1.0 were further reduced to 732 cc/m^2·day and 6.5 g/m^2·day, respectively. The PBAT composite films with enhanced water vapor and water barrier performance exhibit a potential application in green packaging.

Keywords: PBAT; MXene; nanocomposite; gas barrier properties; biaxial stretching

Citation: Wang, X.; Li, X.; Cui, L.; Liu, Y.; Fan, S. Improvement of Gas Barrier Properties for Biodegradable Poly(butylene adipate-co-terephthalate) Nanocomposites with MXene Nanosheets via Biaxial Stretching. *Polymers* **2022**, *14*, 480. https://doi.org/10.3390/polym14030480

Academic Editors: Wei Wu, Hao-Yang Mi, Chongxing Huang, Hui Zhao, Tao Liu and Alexey Iordanskii

Received: 3 December 2021
Accepted: 23 January 2022
Published: 25 January 2022

1. Introduction

Green packaging materials are highly demanded in the recent years because of the ever-increasing plastic pollution problem. The traditional packaging materials, such as polyethylene (PE) and poly(vinyl chloride) (PVC), have been gradually replaced by biodegradable polymers such as poly(lactic acid) (PLA), poly(butylene adipate-co-terephthalate) (PBAT), and poly(butylene succinate) (PBS) [1–4]. Compared with other biodegradable polyesters, PBAT has adjustable properties due to the copolymerization of 1,4-butanediol, adipic acid, and terephthalic acid [5]. In addition, it has good ductility, good thermal resistance, and high impact performance, which is similar to PE. However, it was reported that the oxygen transmission rate (OTR) of PBAT under ambient conditions was around 1050 cc/m^2·day, whereas the water vapor permeability rate (WVPR) was 3.3 × 10^{-11} g·m/m^2·s·Pa, which made it difficult to meet the requirements for packaging applications [6–8]. The poor oxygen and water vapor barrier performances limit the broad applications of PBAT in packaging. Therefore, it is necessary to improve the oxygen and water vapor barrier performance of PBAT so as to prolong the shelf life and maintain good quality of food.

It is widely accepted that the incorporation of nanofillers is a simple and effective method to reduce the OTR and WVPR of polymer films [9–12] because the presence of fillers can have barrier effects that increase the escape distance of oxygen and water molecules [13,14]. Li et al. reported that the well-aligned graphene nanosheets simultaneously reduced the oxygen permeability and enhanced the aging resistance of the PBAT composite film [15]. The oxygen-containing groups on graphene nanosheets enhanced the interactions between water molecules and altered the diffusion paths of water molecules. Mondal et al. found that the WVPR of PBAT could be reduced by 25% with the addition of 4 wt% organically modified montmorillonite (OMMT) [16]. This was because the impermeable OMMT in the PBAT matrix increased the tortuosity of the path for water molecules. Li et al. mixed graphene nanosheets with PBAT by the solution casting method [15]. The presence of graphene resulted in an 80% reduction in water permeation and a 99% reduction in oxygen transmission of PBAT nanocomposite films, which was ascribed to the fact that the graphene nanosheets enlarged the effective diffusion path length of water and oxygen across the films.

MXene is a novel family of (2D) transition metal carbides and/or nitrides [17–21]. The abundance of functional groups on the surface of MXene, such as oxygen (=O), hydroxyl (-OH), or fluorine (-F), endows it with good compatibility with many polar polymer matrices [22]. MXene has attracted considerable research interest for various applications, such as energy storage, sensors, electromagnetic shielding, and so on [23–26]. $Ti_3C_2T_X$ nanosheets have high stiffness and strength, which can serve as effective, reinforced fillers to improve the mechanical properties of polymer/$Ti_3C_2T_X$ nanocomposites. In addition, Wu et al. demonstrated that a small amount of $Ti_3C_2T_X$ improved the complex viscosity and storage modulus of PVDF nanocomposites significantly [22]. The ultrahigh molecular weight polyethylene (UMWPE) composites containing 0.75 wt% $Ti_3C_2T_X$ had the best creep performance [27]. With the addition of 1.9 vol% of MXene, the $Ti_3C_2T_X$/polystyrene nanocomposites exhibited a 54% higher storage modulus than that of neat polystyrene [28]. Yu et al. demonstrated that the addition of MXene improved the thermal stability and fire safety of polystyrene [29]. However, to the best of our knowledge, the PBAT/$Ti_3C_2T_X$ nanocomposites have not been reported on yet. It is expected that the impermeable $Ti_3C_2T_X$ nanosheets in the PBAT matrix via biaxial stretching can not only improve the gas barrier performance, but also enhance the thermal stability and stiffness of the nanocomposites.

Biaxial stretching processing is the process of stretching hot polymeric films in the cross-machine direction. It is also reported that the biaxial stretching process endows the polymer matrix with an ordered structure and improved gas barrier properties [30–32]. This is because the biaxial stretching can help to reduce the free volume of the amorphous region of the polymers, resulting in an enhancement in gas barrier performance [33]. In addition, the biaxial stretching can help the 2D filler in the polymer matrices form an orientation structure, which can benefit for the enhancement of the gas barrier performance [34]. Li et al. reported that the orientated OMMT in the PBAT matrix prepared by biaxial stretching significantly reduced the WVPR and caused a 99% reduction in OTR with an enhancement in elongation at break [15]. Yoksan et al. demonstrated that the stretched PLA/PBAT/thermoplastic starch composite films had stacked-layer planar morphology, which contributed to the improvement in crystallinity, impact strength, water vapor, and oxygen barrier properties [35].

2. Materials and Methods

2.1. Materials

Poly(butylene adipate-co-terephthalate) (PBAT) pellets were supplied by BASF. The melt flow index (190 °C, 2.16 kg) was 5.0 g/10 min. The MXene ($Ti_3C_2T_X$, 400 mesh, purity > 99%) nanosheets etched by HF were supplied by 11 Technology Co., Ltd. (Changchun, China). The specific surface area of the obtained $Ti_3C_2T_X$ was approximately 31.5 m^2/g.

2.2. Preparation of PBAT/$Ti_3C_2T_X$ Nanocomposite Biaxial Stretching Films

The preparation diagram of PBAT/$Ti_3C_2T_X$ nanocomposite biaxial stretching films is shown in Scheme 1. To achieve a better dispersion of $Ti_3C_2T_X$ nanosheets in the PBAT matrix, $Ti_3C_2T_X$ was first mixed with PBAT pellets by melt compounding via a twin extruder to obtain composite casting films. Then the PBAT/$Ti_3C_2T_X$ nanocomposite casting films were biaxially stretched. The effects of $Ti_3C_2T_X$ content on the morphology, thermal stability, and crystallization behavior, as well as mechanical properties of PBAT/$Ti_3C_2T_X$ nanocomposites, were comprehensively evaluated. The PBAT nanocomposite films containing the optimized 1 wt% $Ti_3C_2T_X$ were biaxially stretched under different parameters.

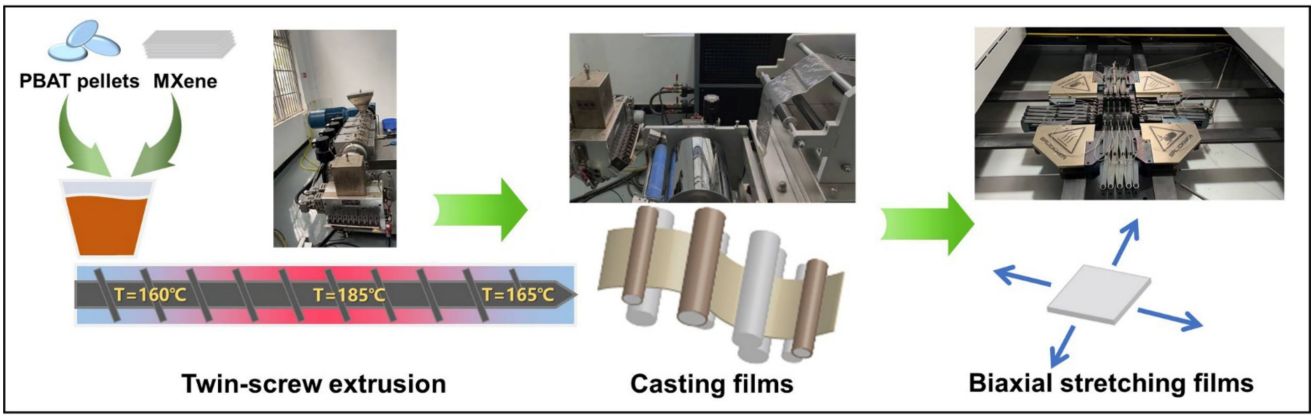

Scheme 1. Schematic diagram of preparation of PBAT/$Ti_3C_2T_X$ nanocomposite biaxial stretching films.

The PBAT/$Ti_3C_2T_X$ nanocomposite biaxial stretching films were prepared by two steps. Prior to the experiment, the PBAT pellets were dried in a vacuum oven at 80 °C for 12 h. Firstly, the PBAT/$Ti_3C_2T_X$ nanocomposite casting film was prepared by extrusion casting (FDHU-35, Potpo, Guangzhou, China) so that the $Ti_3C_2T_X$ could have a better dispersion in the PBAT matrix. The temperatures from the hopper to the nozzle were set at 130-150-170-170-170-150 °C. The screw speed was set at 60 rpm. The thickness of the obtained PBAT/$Ti_3C_2T_X$ nanocomposite casting films was approximately 100 µm. The code of the samples was abbreviated as PBAT-X, where X represents the weight ratio of $Ti_3C_2T_X$ in the PBAT/$Ti_3C_2T_X$ nanocomposites.

The extruded PBAT nanocomposite casting films containing 1 wt% $Ti_3C_2T_X$ nanosheets were cut into squares (80 mm side length) for biaxial stretching. The biaxially oriented films were then prepared at different stretching ratios on a KARO 5.0 (Brückner MaschinenbauGmbH & Co., Siegsdorf, Germany) equipped with mechanically driven clamps. The stretched films were thermally annealed at a temperature of 110 °C for 60 s. Finally, the biaxially oriented nanocomposite films were obtained to characterize the crystal orientation and the gas barrier properties.

2.3. Characterization

The fracture surfaces of the PBAT/$Ti_3C_2T_X$ nanocomposite were characterized by scanning electron microscopy (SEM, Quanta 250, FEI, Hillsboro, OR, USA). The samples were fractured in liquid nitrogen for 30 min. They were observed at an accelerating voltage of 5 kV. Prior to the observation, all the samples were coated with a layer of gold.

Thermogravimetric analysis (TGA) of all PBAT/$Ti_3C_2T_X$ nanocomposites was conducted on a TG-209F1 thermal analyzer (Netzsch, Selb, Germany) to measure the thermal stability under air atmosphere. The samples of about 10 mg were heated from room temperature to 600 °C at a heating rate of 10 °C/min.

The crystallization and melting behaviors of PBAT/$Ti_3C_2T_X$ nanocomposites were conducted on a DSC-204F1 (Netzsch, Selb, Germany). The samples of approximately 5 mg were first heated to 180 °C at a heating rate of 10 °C/min to establish the thermal history, then cooled to 20 °C at a cooling rate of 10 °C/min and followed by a second heating

rate of 10 °C/min to 180 °C. The peak crystallization temperature (T_{cp}), the peak melting temperature (T_{mp}), the crystallization enthalpy (ΔH_c), and the melting enthalpy (ΔH_m) of these samples were summarized. The degree of crystallinity of PBAT (χ_c) was calculated by the following equation:

$$\chi_c = \frac{\Delta H_m}{\Delta H_0(1-\varphi_c)} \quad (1)$$

where ΔH_0 is the 100% melting enthalpy of PBAT (114 J/g) [36], and φ_c presents the weight ratio of $Ti_3C_2T_X$ in the nanocomposites.

The tensile test was performed on an Instron 5566 universal electron tensile machine. The specimens were cut into rectangle shape with a dimension of 1 cm × 8 cm × 100 µm. The tensile speed was fixed at 10 mm/min. The reported results were the average values of at least five successful specimens.

The dynamical mechanical analysis was conducted on a Netzsch DMA 242E (Netzsch, Selb, Germany) analyzer. Tensile measurements were taken on specimens with dimensions of 30 mm at a fixed frequency of 1 Hz and from 90 °C to 70 °C at a ramping rate of 3 °C/min.

The 2D, wide-angle, X-ray scattering (2D-WAXS) measurements were carried out on an X-ray diffractometer (Rigaku UltimaIV, The Woodlands, TX, USA). The data were collected in the scanning range of 10–60° with a step of 0.02°.

The oxygen transmission rate (OTR) of the oriented films was measured with a MOCON OX-TRAN (Ametek Mocon, Brooklyn Park, MN, USA) 2/21 at 23 °C, 1 atm, and 85% RH. The water vapor transmission rate (WVTR) was determined according to ASTM E96-80 at MOCON PERMATRAN-W 3/33 (Ametek Mocon, Brooklyn Park, MN, USA). The reported values were the average results of three successful samples.

3. Results and Discussions

3.1. Morphology

Figure 1 shows the SEM images of the cross-section fracture surfaces of PBAT/$Ti_3C_2T_X$ nanocomposite films. In Figure 1a,b, PBAT-0 exhibits a relatively smooth surface due to its brittle fracture after immersion in liquid nitrogen [37]. With the addition of $Ti_3C_2T_X$ nanosheets, the surfaces of the PBAT/$Ti_3C_2T_X$ nanocomposites become gradually rough in Figure 1c–f when the $Ti_3C_2T_X$ content is lower than 2.0 wt%. This is due to the presence of $Ti_3C_2T_X$, which served as a rigid filler to transfer the stress during facture. In addition, it can be seen that an agglomeration phenomenon existed on the surface of PBAT-2.0 (Figure 1g,h). In Figure 1, no pores and holes are observable between the exposed $Ti_3C_2T_X$ nanosheets on the surfaces (Figure 1f,h) and the PBAT matrix, indicating that $Ti_3C_2T_X$ nanosheets have good compatibility with the PBAT matrix. It is attributed to the large number of polar groups of $Ti_3C_2T_X$ that can react with the polyester groups of PBAT.

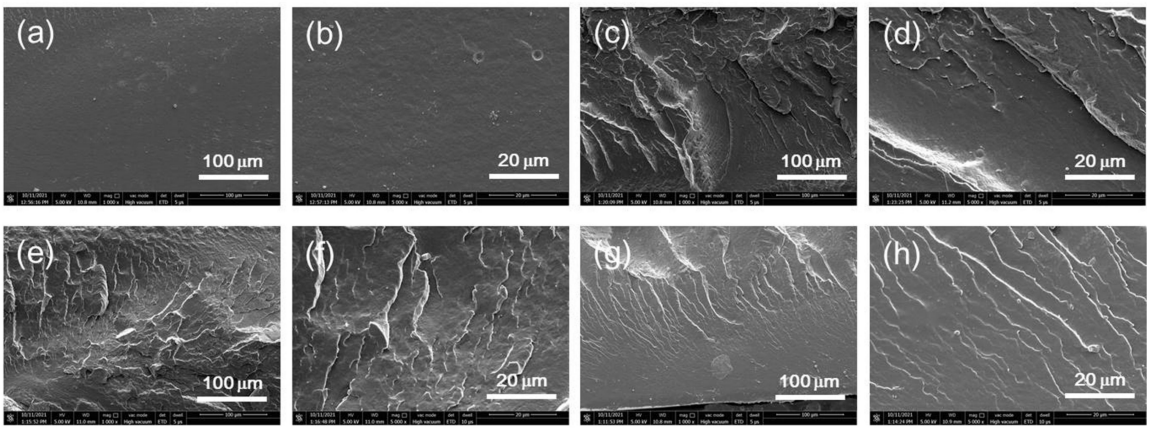

Figure 1. SEM images of the cross-section PBAT/$Ti_3C_2T_X$ nanocomposite films. (**a**,**b**) PBAT-0, (**c**,**d**) PBAT-0.5, (**e**,**f**) PBAT-1.0, and (**g**,**h**) PBAT-2.0.

3.2. Thermal Stability

The thermal stability of PBAT/$Ti_3C_2T_X$ nanocomposites is shown in Figure 2, and the corresponding data, including the temperatures at 10% weight loss (T_{10}), the temperatures at the maximum weight loss rate (T_{max}), and the char yields at 600 °C, are listed in Table 1. In Figure 2a, two thermal decomposition stages are observable for all the samples. The first stage between 300 °C and 420 °C can be attributed to the random, main-chain scission and thermo-oxidative reactions of PBAT [38]. The second stage, in the range of 420–550 °C, corresponds to cis-elimination and thermo-oxidative reactions [32]. In Table 1, it can be seen that the values of T_{10} showed an increasing trend with the increase of $Ti_3C_2T_X$ content. When compared to PBAT-0, the T_{10} of PBAT-2.0 dropped from 373.5 °C to 379.2 °C. In addition, the T_p of PBAT-2.0 gradually increased to 412.5 °C with the addition of 2 wt% $Ti_3C_2T_X$. That is because the presence of $Ti_3C_2T_X$ rapidly catalyzed the formation of a char layer that served as a thermal barrier to protect the underlying polymer matrices [39]. The improvement of char yield benefited from the isolating of volatile gases and oxygen; therefore, improving the thermal stability of PBAT. Furthermore, the char yield at 600 °C for PBAT-0, PBAT-0.5, PBAT-1.0, and PBAT-2.0 was 0.7%, 1.0%, 1.4%, and 1.7%, respectively. It was mainly due to the introduction of $Ti_3C_2T_X$, which promoted charring, and partial polymers could not be completely thermally decomposed, resulting in enhanced char residues [40].

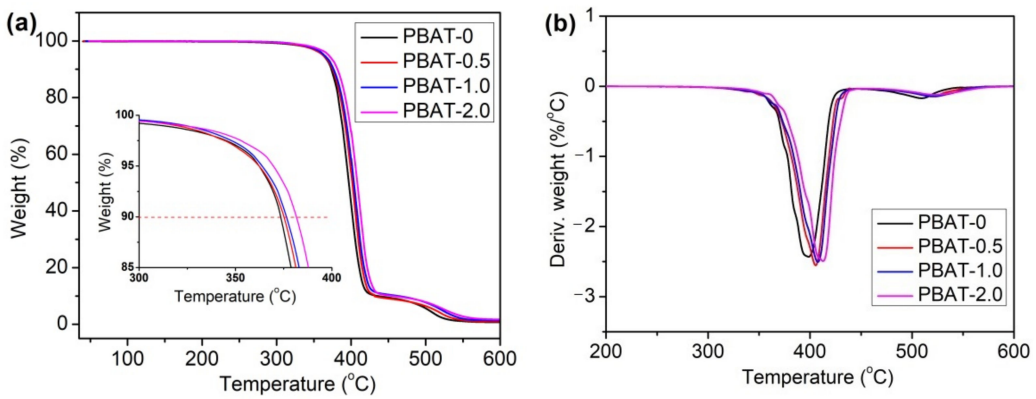

Figure 2. TGA curves of PBAT/$Ti_3C_2T_X$ nanocomposites at air atmospheres. (**a**) TGA and (**b**) DTG.

Table 1. Thermal stability of PBAT/$Ti_3C_2T_X$ nanocomposite films.

Samples	T_{10} (°C)	T_p (°C)	Char Yield at 600 °C (wt%)
PBAT-0	373.5	398.3	0.7
PBAT-0.5	375.1	404.7	1.0
PBAT-1.0	376.4	408.5	1.4
PBAT-2.0	379.2	412.5	1.7

3.3. Crystallization and Melting Behavior

The DSC curves of the PBAT/$Ti_3C_2T_X$ nanocomposites are shown in Figure 3. In Figure 3a, the onset crystallization temperatures of PBAT nanocomposites exhibit an increasing trend with the increase of $Ti_3C_2T_X$ content. In addition, the values of T_{cp} for PBAT nanocomposites in Table 2 are 72.1, 73.1, 73.7, and 75.2 °C, respectively. The increase in T_{cp} indicated that the presence of $Ti_3C_2T_X$ had a heterogeneous nucleation effect, accelerating the formation of crystallites in the PBAT matrix during cooling [41]. It was noted that the values of ΔH_m were lower than ΔH_c for the PBAT/$Ti_3C_2T_X$ composites, which can be ascribed to the fast cooling rate. In Figure 3b, the values of T_{mp} for PBAT nanocomposites are 119.3, 121.0, 121.6, and 121.0 °C, respectively. The increase in T_{mp} suggests that the filling $Ti_3C_2T_X$ contributes to the formation of perfect crystallinity of PBAT during the cooling procedure. Moreover, the crystallization degree of PBAT-1.0 had the highest value of 13.4% with the addition of 1.0 wt% $Ti_3C_2T_X$. When the content of $Ti_3C_2T_X$ was further increased up to 2.0 wt%, the crystallization degree of PBAT-2.0 showed a slight decrease.

This may be due to the excessive addition of $Ti_3C_2T_X$, which led to agglomeration, to some extent. On the other hand, the inhibition effects of the excessive $Ti_3C_2T_X$ nanosheets were more profound than the nucleating effect that led to smaller crystallization and decreased crystallinity [42].

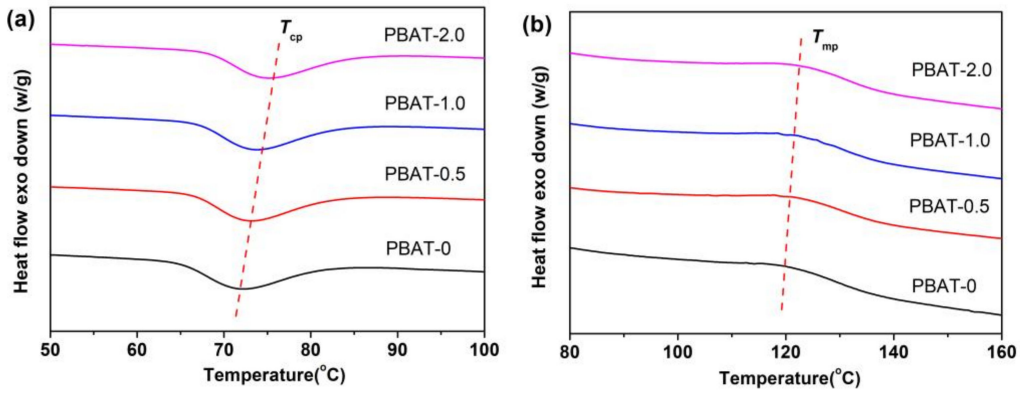

Figure 3. Differential scanning calorimetry (DSC) thermograms of PBAT/$Ti_3C_2T_X$ nanocomposites. (**a**) first cooling, (**b**) second heating.

Table 2. DSC thermograms of PBAT/$Ti_3C_2T_X$ nanocomposites.

Samples	T_{cp} (°C)	ΔH_c (J/g)	T_{mp} (°C)	ΔH_m (J/g)	χ (%)
PBAT-0	72.1	16.8	119.3	14.6	12.8
PBAT-0.5	73.1	17.0	121.0	14.7	13.0
PBAT-1.0	73.7	16.8	121.6	15.1	13.4
PBAT-2.0	75.2	16.9	121.0	14.2	12.7

3.4. Mechanical Properties of Casting Films

Figure 4 shows the typical stress–strain curves for pure PBAT and PBAT/$Ti_3C_2T_X$ nanocomposite casting films, and the corresponding data are summarized in Table 3. It was observed that PBAT-0 exhibited a high ductility (elongation at break ~ 1442%) but low tensile strength (~22.6 MPa), which is consistent with previous report [14]. With the addition of 0.5 wt% $Ti_3C_2T_X$, the tensile strength of the PBAT/$Ti_3C_2T_X$ nanocomposite increased by 19.8% with a slight increase in the elongation at break. As depicted in Figure 1, the $Ti_3C_2T_X$ had good interfacial interaction with the PBAT matrix; therefore, the addition of $Ti_3C_2T_X$ nanosheets can transform the stress during the tensile process. When the $Ti_3C_2T_X$ content was increased to 1.0%, the PBAT/$Ti_3C_2T_X$ nanocomposite had the maximum tensile strength (31.6 MPa). This enhancement can be ascribed to the reinforcement effects of the nanofillers and the interaction between the stress concentration zones around the $Ti_3C_2T_X$ nanosheets [43,44]. It is worth noting that PBAT-2.0 showed a decreasing tendency in both tensile stress and elongation at break as compared with PBAT-1.0. This may be due to the aggregation of $Ti_3C_2T_X$ nanosheets in the PBAT matrix.

Table 3. Tensile properties of PBAT/$Ti_3C_2T_X$ nanocomposite casting films.

Samples	Tensile Stress (MPa)	Young's Modulus (MPa)	Elongation at Break (%)
PBAT-0	22.6 ± 3.2	24.5 ± 4.1	1442.3 ± 104.5
PBAT-0.5	27.1 ± 3.6	28.6 ± 2.0	1524.8 ± 98.7
PBAT-1.0	31.6 ± 4.7	31.4 ± 2.9	1483.2 ± 132.4
PBAT-2.0	24.3 ± 5.1	32.1 ± 3.3	1350.3 ± 329.7

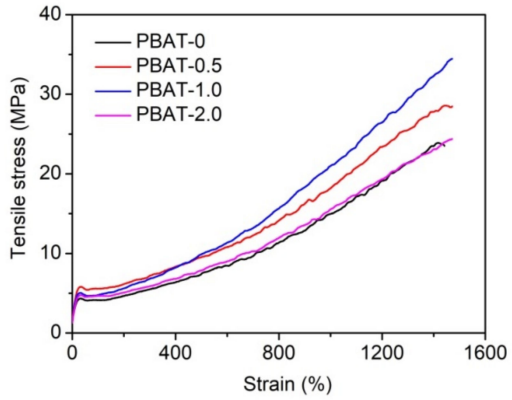

Figure 4. Tensile stress versus strain of PBAT/$Ti_3C_2T_X$ nanocomposite casting films.

3.5. Dynamic Mechanical Analysis

The storage modulus as a function of temperature for PBAT/$Ti_3C_2T_X$ nanocomposite casting films is shown in Figure 5a. It is clear that the storage modulus of the PBAT nanocomposite reinforced with $Ti_3C_2T_X$ was higher than that of PBAT-0 in the glassy states. In addition, the reinforcement effect was more obvious with the increase of $Ti_3C_2T_X$ content. When compared to PBAT-0, the storage modulus of PBAT-2.0 at 80 °C increased from 1220 MPa to 2342 MPa. This is due to the stiffening effect of rigid $Ti_3C_2T_X$ nanosheets. Aside from this, the polar groups on the surface of $Ti_3C_2T_X$ may have had intramolecular interaction with the PBAT. matrix, which may have also improved the storage modulus of the PBAT/$Ti_3C_2T_X$ nanocomposites [43]. The loss factor peak (tanδ) is usually defined as the glass transition temperature (T_g). It is observable from Figure 5b that the T_g shifted to a lower temperature when the PBAT matrix was incorporated with $Ti_3C_2T_X$. With the addition of 2 wt% $Ti_3C_2T_X$, the PBAT-2.0 shifted from −11.9 °C to −15.0 °C, as compared with that of PBAT-0. It can be attributed to the incorporation of $Ti_3C_2T_X$, which can improve the chain mobility of the amorphous regions of PBAT due to the liberation effect of $Ti_3C_2T_X$. In addition, the height of tanδ also showed a slight increase, indicating that an increase in $Ti_3C_2T_X$ content will result in higher dissipative energy [45].

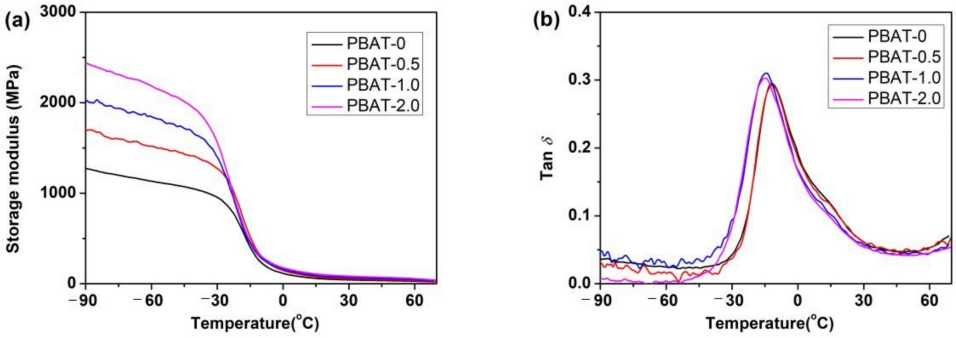

Figure 5. (**a**) Storage modulus and (**b**) loss factor of PBAT/$Ti_3C_2T_X$ nanocomposite casting films.

3.6. 2D-WAXS Patterns of Biaxial Stretching Films

Figure 6 shows the 2D-WAXS images of the PBAT-1.0 casting films under different biaxial stretching ratios. It is observable that there are four crystal planes (111), (100), (110), and (010) in the PBAT film (1 × 1) in Figure 6a, and these crystal planes belong to the PBAT phase [10]. With the increase of the stretching ratio in the machine direction (MD), the crystal planes (111), (100), (110), and (010) in the PBAT composite films (Figure 6b,c) had more obvious orientation. In addition, the larger the stretching ratio, the more obvious the orientation effect, which indicates that uniaxial stretching can promote the orientation of the PBAT/$Ti_3C_2T_X$ biaxial stretching films' crystal form along the MD. In Figure 6d,e,

there is no obvious crystal orientation in the 2D-WAXS diffraction pattern in the biaxially stretched PBAT/$Ti_3C_2T_X$ films, indicating that the biaxial stretching will not cause the film to have an obvious crystal orientation in a certain direction. The crystal orientation of PBAT/$Ti_3C_2T_X$ composite films further confirms that the biaxially oriented PBAT/$Ti_3C_2T_X$ film has excellent isotropy.

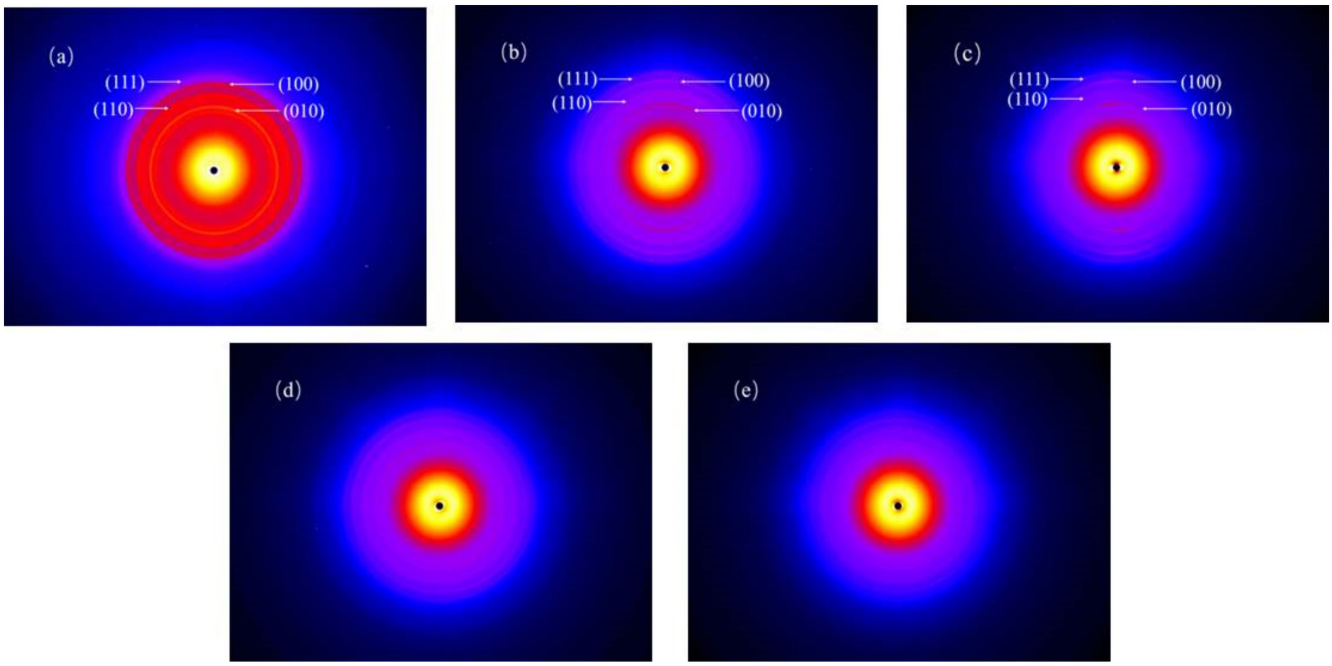

Figure 6. The films of PBAT-1.0 under different biaxial stretching ratio (transverse direction × machine direction). (**a**) 1 × 1, (**b**) 1 × 2, (**c**) 1 × 3, (**d**) 1.5 × 1.5, and (**e**) 2 × 2.

3.7. Gas Barrier Properties of Biaxial Stretching Films

The gas barrier properties of PBAT/$Ti_3C_2T_X$ nanocomposite casting films are shown in Figure 7. In Figure 7a, the OTR of PBAT nanocomposite casting films shows a decreasing trend with the increase of $Ti_3C_2T_X$ content. The lowest OTR was achieved for PBAT-1.0, which decreased from 1030 to 782 cc/m^2·day. Similarly, the water vapor transmission rate (WVTR) of PBAT/$Ti_3C_2T_X$ nanocomposite casting films decreased as the $Ti_3C_2T_X$ content increased in the PBAT matrix. In Figure 7b, the WVTR for PBAT-0, PBAT-0.5, PBAT-1.0, and PBAT-2.0 is determined to be 14.3, 12.7, 10.2, and 11.7 g/m^2·day, respectively. It is speculated that the addition of $Ti_3C_2T_X$ nanosheets can serve as a barrier to form a tortuous path, increasing the effective diffusion path length. Furthermore, the abundant hydroxyl groups on the surface of $Ti_3C_2T_X$ will contribute to the interactions with water molecules, delaying the diffusion to some extent. However, the aggregation of $Ti_3C_2T_X$ will result in a deterioration of the gas barrier performance when the content of $Ti_3C_2T_X$ is increased by up to 2.0 wt%.

To investigate the effects of the stretching ratio on the gas barrier performance of PBAT/$Ti_3C_2T_X$ nanocomposite stretching films, the OTR and WVTR data of PBAT-1.0 stretching film under different stretching ratios are shown in Figure 8. In Figure 8a, it is clear that the OTR of PBAT-1.0 stretching film decreased from 782 to 732 cc/m^2·day with the stretching ratio increasing to 3 under uniaxial stretching. This can be attributed to the enhanced orientation of PBAT crystallites formed during the uniaxial stretching process, which is demonstrated in 2D-WAXS patterns (Figure 6). Meanwhile, the WVTR for PBAT-1.0 stretching film achieved the lowest value of 6.5 g/m^2·day under 2 × 2 biaxial stretching condition, shown in Figure 8b. This is because the biaxial stretching process can contribute to the formation of an amorphous phase of PBAT and the exfoliation of $Ti_3C_2T_X$ sheets. However, the barrier effect of $Ti_3C_2T_X$ sheets is more profound than the effect of the PBAT

amorphous phase, resulting in a further decrease in OTR and WVTR. The combination of two-dimensional, inorganic nanofillers with the biaxial stretching process paves the way for the preparation of a biodegradable polymer with enhanced gas barrier performance.

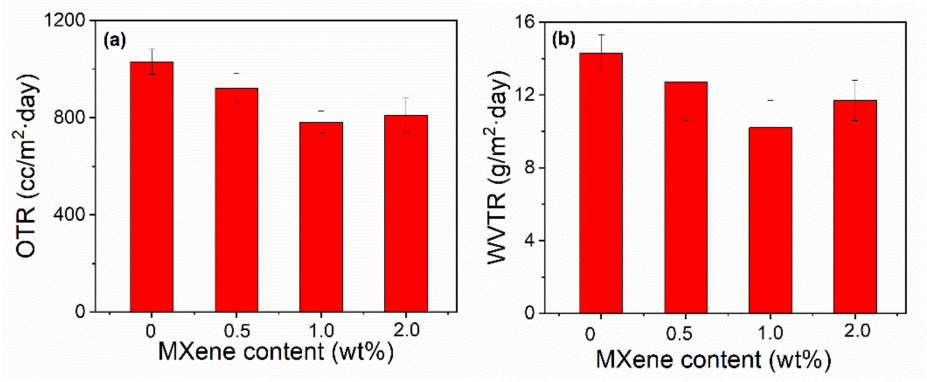

Figure 7. The gas barrier properties of PBAT/$Ti_3C_2T_X$ nanocomposite casting films. (**a**) OTR, (**b**) WVTR.

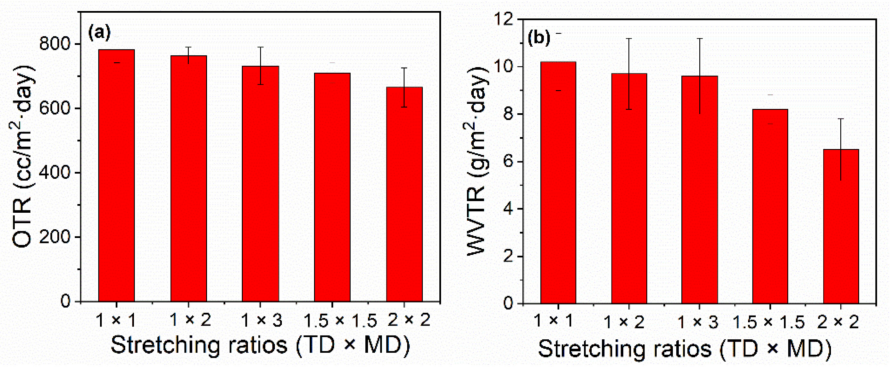

Figure 8. The gas barrier properties of PBAT-1.0 films under different biaxial stretching ratio. (**a**) OTR, (**b**) WVTR.

4. Conclusions

In this work, two-dimensional MXene ($Ti_3C_2T_X$) nanosheets were mixed with PBAT by melt compounding. The effects of $Ti_3C_2T_X$ content on the morphology, thermal stability, crystallization behavior, and gas barrier performance of PBAT were investigated. Furthermore, the effects of the biaxial stretching ratio on the gas barrier properties were further discussed. The TGA results showed that the addition of $Ti_3C_2T_X$ improved the thermal stability of the PBAT nanocomposite. In addition, the tensile tests showed that the addition of 1.0 wt% $Ti_3C_2T_X$ improved the maximum tensile stress without losing ductility. The storage modulus of PBAT was significantly improved in the glassy state with the addition of $Ti_3C_2T_X$. After biaxial stretching, the PBAT-1.0 film (1 × 3) exhibited an oxygen transmission rate of 732 cc/m^2·day, which was 28.9% lower than that of pure PBAT casting film. When the stretching ratio was 2 × 2, the WVTR of PBAT-1.0 biaxial stretching film was 6.5 g/m^2·day, which was 36.3% lower than that of 1 × 1 PBAT-1.0 film. The enhancement in gas barrier properties can be attributed to the presence of $Ti_3C_2T_X$ nanosheets, which can increase the effective diffusion path length for gases. The results of this work indicate the need for further studies on the influence of the orientation and surface functionalization of $Ti_3C_2T_X$ nanosheets, as well as the incorporation of compatbilizers in the PBAT composite films for packaging applications.

Author Contributions: Investigation, X.W., X.L., L.C. and S.F.; writing—original draft preparation, X.W. and X.L.; methodology, X.W. and X.L.; writing—review and editing, Y.L. and S.F.; supervision, Y.L. and S.F. All authors have read and agreed to the published version of the manuscript.

Funding: This research was funded by the Natural Science Foundation of Hunan Province (no. 2019JJ50132) and the Innovation Platform Open Fund of Hunan Province (no. 18K079).

Institutional Review Board Statement: This study did not involve humans or animals.

Informed Consent Statement: This study did not involve patients.

Data Availability Statement: The raw/processed data required to reproduce these findings cannot be shared at this time as the data also form part of an ongoing study.

Conflicts of Interest: The authors declare no conflict of interest.

References

1. Ellingford, C.; Samantaray, P.K.; Farris, S.; McNally, T.; Tan, B.W.; Sun, Z.Y.; Huang, W.J.; Ji, Y.; Wan, C.Y. Reactive extrusion of biodegradable PGA/PBAT blends to enhance flexibility and gas barrier properties. *J. Appl. Polym. Sci.* **2021**, *139*, e51617. [CrossRef]
2. Cao, X.W.; Chi, X.N.; Deng, X.Q.; Sun, Q.J.; Gong, X.J.; Yu, B.; Yuen, A.C.Y.; Wu, W.; Li, R.K.Y. Facile synthesis of phosphorus and cobalt co-doped graphitic carbon nitride for fire and smoke suppressions of polylactide composite. *Polymers* **2020**, *12*, 1106. [CrossRef]
3. Karkhanis, S.S.; Stark, N.M.; Sabo, R.C.; Matuana, L.M. Potential of extrusion-blown poly(lactic acid)/cellulose nanocrystals nanocomposite films for improving the shelf-life of a dry food product. *Food Packag. Shelf Life* **2021**, *29*, 100689. [CrossRef]
4. Cao, X.W.; Huang, J.S.; He, Y.; Hu, C.Y.; Zhang, Q.C.; Yin, X.M.; Wu, W.; Li, R.K.Y. Biodegradable and renewable UV-shielding polylactide composites containing hierarchical structured POSS functionalized lignin. *Int. J. Biol. Macromol.* **2021**, *188*, 323–332. [CrossRef]
5. Huang, F.F.; Wu, L.B.; Li, B.G. Sulfonated biodegradable PBAT copolyesters with improved gas barrier properties and excellent water dispersibility: From synthesis to structure-property. *Polym. Degrad. Stab.* **2020**, *182*, 109391. [CrossRef]
6. Venkatesan, R.; Rajeswari, N. ZnO/PBAT nanocomposite films: Investigation on the mechanical and biological activity for food packaging. *Polym. Adv. Technol.* **2017**, *28*, 20–27. [CrossRef]
7. Li, J.X.; Lai, L.; Wu, L.B.; Severtson, S.J.; Wang, W.J. Enhancement of water vapor barrier properties of biodegradable poly(butylene adipate-co-terephthalate) films with highly oriented organomontmorillonite. *ACS Sustain. Chem. Eng.* **2018**, *6*, 6654–6662. [CrossRef]
8. Bumbudsanpharoke, N.; Wongphan, P.; Promhuad, K.; Leelaphiwat, P.; Harnkarnsujarit, N. Morphology and permeability of bio-based poly (butylene adipate-co-terephthalate)(PBAT), poly (butylene succinate)(PBS) and linear low-density polyethylene (LLDPE) blend films control shelf-life of packaged bread. *Food Control* **2021**, *132*, 108541. [CrossRef]
9. Botta, L.; Titone, V.; Mistretta, M.C.; La Mantia, F.P.; Modica, A.; Bruno, M.; Sottile, F.; Lopresti, F. PBAT based composites reinforced with microcrystalline cellulose obtained from softwood almond shells. *Polymers* **2021**, *13*, 2643. [CrossRef]
10. Ren, P.G.; Liu, X.H.; Ren, F.; Zhong, G.J.; Ji, X.; Xu, L. Biodegradable graphene oxide nanosheets/poly-(butylene adipate-coterephthalate) nanocomposite film with enhanced gas and water vapor barrier properties. *Polym. Test.* **2017**, *58*, 173–180. [CrossRef]
11. Yao, Q.R.; Song, Z.Y.; Li, J.; Zhang, L. Micromorphology, mechanical, crystallization and permeability properties analysis of HA/PBAT/PLA (HA, hydroxyapatite; PBAT, poly(butylene adipate-co-butylene terephthalate); PLA, polylactide) degradability packaging films. *Polym. Int.* **2020**, *69*, 301–307. [CrossRef]
12. Sangroniz, A.; Sangroniz, L.; Gonzalez, A.; Santamaria, A.; del Rio, J.; Iriarte, M.; Etxeberria, A. Improving the barrier properties of a biodegradable polyester for packaging applications. *Eur. Polym. J.* **2019**, *115*, 76–85. [CrossRef]
13. Wadaugsorn, K.; Panrong, T.; Wongphan, P.; Harnkarnsujarit, N. Plasticized hydroxypropyl cassava starch blended PBAT for improved clarity blown films: Morphology and properties. *Ind. Crops Prod.* **2022**, *176*, 114311. [CrossRef]
14. Qin, P.K.; Wu, L.B.; Li, B.G.; Li, N.X.; Pan, X.H.; Dai, J.M. Superior gas barrier properties of biodegradable PBST vs. PBAT copolyesters: A comparative study. *Polymers* **2021**, *13*, 3449. [CrossRef]
15. Li, J.X.; Wang, S.L.; Lai, L.; Liu, P.W.; Wu, H.Q.; Xu, J.L.; Severtson, S.J.; Wang, W.J. Synergistic enhancement of gas barrier and aging resistance for biodegradable films with aligned graphene nanosheets. *Carbon* **2021**, *172*, 31–40. [CrossRef]
16. Mondal, D.; Bhowmick, B.; Mollick, M.M.R.; Maity, D.; Saha, N.R.; Rangarajan, V.; Rana, D.; Sen, R.; Chattopadhyay, D. Antimicrobial activity and biodegradation behavior of poly(butylene adipate-co-terephthalate)/clay nanocomposites. *J. Appl. Polym. Sci.* **2014**, *131*, 40079. [CrossRef]
17. Gao, L.F.; Li, C.; Huang, W.C.; Mei, S.; Lin, H.; Ou, Q.; Zhang, Y.; Guo, J.; Zhang, F.; Xu, S.X.; et al. MXene/polymer membranes: Synthesis, properties, and emerging applications. *Chem. Mater.* **2020**, *32*, 1703–1747. [CrossRef]
18. Anasori, B.; Lukatskaya, M.R.; Gogotsi, Y. 2D metal carbides and nitrides (MXenes) for energy storage. *Nat. Rev. Mater.* **2017**, *2*, 16098. [CrossRef]
19. Sun, Z.M. Progress in research and development on MAX phases: A family of layered ternary compounds. *Int. Mater. Rev.* **2011**, *56*, 143–166. [CrossRef]
20. Ihsanullah, I. MXenes (two-dimensional metal carbides) as emerging nanomaterials for water purification: Progress, challenges and prospects. *Chem. Eng. J.* **2020**, *388*, 124340. [CrossRef]

21. Ihsanullah, I. Potential of MXenes in water desalination: Current status and perspectives. *Nano-Micro Lett.* **2020**, *12*, 1–20. [CrossRef]
22. Wu, W.; Zhao, W.J.; Sun, Q.J.; Yu, B.; Yin, X.M.; Cao, X.W.; Feng, Y.H.; Li, R.K.Y.; Qu, J.P. Surface treatment of two dimensional MXene for poly(vinylidene fluoride) nanocomposites with tunable dielectric permittivity. *Compos. Commun.* **2021**, *23*, 100562. [CrossRef]
23. Nan, J.X.; Guo, X.; Xiao, J.; Li, X.; Chen, W.H.; Wu, W.J.; Liu, H.; Wang, Y.; Wu, M.H.; Wang, G.X. Nanoengineering of 2D MXene-based materials for energy storage applications. *Small* **2021**, *17*, 1902085. [CrossRef]
24. Liu, C.; Wu, W.; Shi, Y.Q.; Yang, F.Q.; Liu, M.H.; Chen, Z.X.; Yu, B.; Feng, Y.Z. Creating MXene/reduced graphene oxide hybrid towards highly fire safe thermoplastic polyurethane nanocomposites. *Compos. Part B-Eng.* **2020**, *203*, 108486. [CrossRef]
25. Lan, C.T.; Jia, H.; Qiu, M.H.; Fu, S.H. Ultrathin MXene/polymer coatings with an alternating structure on fabrics for enhanced electromagnetic interference shielding and fire-resistant protective performances. *ACS Appl. Mater. Interfaces* **2021**, *13*, 38761–38772. [CrossRef]
26. Wang, Z.X.; Han, X.S.; Zhou, Z.J.; Meng, W.Y.; Han, X.W.; Wang, S.J.; Pu, J.W. Lightweight and elastic wood-derived composites for pressure sensing and electromagnetic interference shielding. *Compos. Sci. Technol.* **2021**, *213*, 108931. [CrossRef]
27. Zhang, H.; Wang, L.B.; Chen, Q.; Li, P.; Zhou, A.G.; Cao, X.X.; Hu, Q.K. Preparation, mechanical and anti-friction performance of MXene/polymer composites. *Mater. Des.* **2016**, *92*, 682–689. [CrossRef]
28. Sun, R.H.; Zhang, H.B.; Liu, J.; Xie, X.; Yang, R.; Li, Y.; Hong, S.; Yu, Z.Z. Highly conductive transition metal carbide/carbonitride(MXene)@polystyrene nanocomposites fabricated by electrostatic assembly for highly efficient electromagnetic interference shielding. *Adv. Funct. Mater.* **2017**, *27*, 1702807. [CrossRef]
29. Yu, B.; Yuen, A.C.Y.; Xu, X.D.; Zhang, Z.C.; Yang, W.; Lu, H.D.; Fei, B.; Yeoh, G.H.; Song, P.A.; Wang, H. Engineering MXene surface with POSS for reducing fire hazards of polystyrene with enhanced thermal stability. *J. Hazard. Mater.* **2021**, *401*, 123342. [CrossRef]
30. Gao, H.W.; Cao, W.K.; He, J.M.; Bai, Y.P. Highly transparent biaxially oriented poly(ester amide) film with improved gas barrier properties and good mechanical strength. *Eur. Polym. J.* **2021**, *156*, 110620. [CrossRef]
31. Kanai, T.; Okuyama, Y.; Takashige, M. Dynamics and structure development for biaxial stretching PA6/MXD6 blend packaging films. *Adv. Polym. Technol.* **2018**, *37*, 2828–2837. [CrossRef]
32. Jung, B.N.; Jung, H.W.; Kang, D.H.; Kim, G.H.; Shim, J.K. A study on the oxygen permeability behavior of nanoclay in a polypropylene/nanoclay nanocomposite by biaxial stretching. *Polymers* **2021**, *13*, 2760. [CrossRef] [PubMed]
33. Kim, D.Y.; Lee, J.B.; Lee, D.Y.; Seo, K.H. Plasticization effect of poly(lactic acid) in the poly(butylene adipate-co-terephthalate) blown film for Tear resistance improvement. *Polymers* **2020**, *12*, 1904. [CrossRef] [PubMed]
34. Wu, F.; Misra, M.; Mohanty, A.K. Challenges and new opportunities on barrier performance of biodegradable polymers for sustainable packaging. *Prog. Polym. Sci.* **2021**, *117*, 101395. [CrossRef]
35. Yoksan, R.; Dang, K.M.; Boontanimitr, A.; Chirachanchai, S. Relationship between microstructure and performances of simultaneous biaxially stretched films based on thermoplastic starch and biodegradable polyesters. *Int. J. Biol. Macromol.* **2021**, *190*, 141–150. [CrossRef]
36. Wang, X.G.; Cui, L.N.; Fan, S.H.; Li, X.; Liu, Y.J. Biodegradable poly(butylene adipate-co-terephthalate) antibacterial nanocomposites reinforced with MgO nanoparticles. *Polymers* **2021**, *13*, 507. [CrossRef] [PubMed]
37. Wu, W.; Cao, X.W.; Luo, J.; He, G.J.; Zhang, Y.J. Morphology, thermal, and mechanical properties of poly(butylene succinate) reinforced with halloysite nanotube. *Polym. Compos.* **2014**, *35*, 847–855. [CrossRef]
38. Al-Itry, R.; Lamnawar, K.; Maazouz, A. Improvement of thermal stability, rheological and mechanical properties of PLA, PBAT and their blends by reactive extrusion with functionalized epoxy. *Polym. Degrad. Stab.* **2012**, *97*, 1898–1914. [CrossRef]
39. Wu, W.; Zhao, W.J.; Gong, X.J.; Sun, Q.J.; Cao, X.W.; Su, Y.J.; Yu, B.; Li, R.K.Y.; Vellaisamy, R.A.L. Surface decoration of halloysite nanotubes with POSS for fire-safe thermoplastic polyurethane nanocomposites. *J. Mater. Sci. Technol.* **2022**, *101*, 107–117. [CrossRef]
40. Sheng, X.X.; Li, S.H.; Zhao, Y.F.; Zhai, D.S.; Zhang, L.; Lu, X. Synergistic effects of two-dimensional MXene and ammonium polyphosphate on enhancing the fire safety of polyvinyl alcohol composite aerogels. *Polymers* **2019**, *11*, 1964. [CrossRef]
41. Xiong, S.J.; Bo, P.; Zhou, S.J.; Li, M.K.; Yang, S.; Wang, Y.Y.; Shi, Q.T.; Wang, S.F.; Yuan, T.Q.; Sun, R.C. Economically competitive biodegradable PBAT/lignin composites: Effect of lignin methylation and compatibilizer. *ACS Sustain. Chem. Eng.* **2020**, *8*, 5338–5346. [CrossRef]
42. Yan, D.S.; Wang, Z.Y.; Guo, Z.Y.; Ma, Y.M.; Wang, C.Y.; Tan, H.Y.; Zhang, Y.H. Study on the properties of PLA/PBAT composite modified by nanohydroxyapatite. *J. Mater. Res. Technol.* **2020**, *9*, 11895–11904. [CrossRef]
43. Kargarzadeh, H.; Galeski, A.; Pawlak, A. PBAT green composites: Effects of kraft lignin particles on the morphological, thermal, crystalline, macro and micromechanical properties. *Polymer* **2020**, *203*, 122748. [CrossRef]
44. Blyakhman, F.A.; Makarova, E.B.; Fadeyev, F.A.; Lugovets, D.V.; Safronov, A.P.; Shabadrov, P.A.; Shklyar, T.F.; Melnikov, G.Y.; Orue, I.; Kurlyandskaya, G.V. The contribution of magnetic nanoparticles to ferrogel biophysical properties. *Nanomaterials* **2019**, *9*, 232. [CrossRef]
45. Jaszkiewicz, A.; Bledzki, A.K.; Meljon, A. Dynamic mechanical thermal analysis of biocomposites based on PLA and PHBV-A comparative study to PP counterparts. *J. Appl. Polym. Sci.* **2013**, *130*, 3175–3183.